Core-Shell Plasmonic Nanohelices

Kosters, Dolfine; De Hoogh, Anouk; Zeijlemaker, Hans; Acar, Hakkl; Rotenberg, Nir; Kuipers, L.

DOI
10.1021/acsphotonics.7b00496

Publication date
2017

Document Version
Final published version

Published in
ACS Photonics

ACS Photonics

Article

pubs.acs.org/journal/apchd5

Core−Shell Plasmonic Nanohelices

Dolfine Kosters,[†,‡] Anouk de Hoogh,[‡] Hans Zeijlemaker,[‡] Hakkı Acar,[‡] Nir Rotenberg,[§] and L. Kuipers*[,†,‡]

[†]Kavli Institute of Nanoscience, Department for Quantum Nanoscience, Lorentzweg 1, 2628 CJ Delft, The Netherlands

[‡]Center for Nanophotonics, AMOLF, Science Park 104, 1098 XG Amsterdam, The Netherlands

[§]Max Planck Institute for the Science of Light, Staudtstraße 2, D-91058 Erlangen, Germany

Supporting Information

ABSTRACT: We introduce core−shell plasmonic nanohelices, highly tunable structures that have a different response in the visible for circularly polarized light of opposite handedness. The glass core of the helices is fabricated using electron beam induced deposition and the pure gold shell is subsequently sputter coated. Optical measurements allow us to explore the chiral nature of the nanohelices, where differences in the response to circularly polarized light of opposite handedness result in a dissymmetry factor of 0.86, more than twice of what has been previously reported. Both experiments and subsequent numerical simulations demonstrate the extreme tunability of the core−shell structures, where nanometer changes to the geometry can lead to drastic changes of the optical responses. This tunability, combined with the large differential transmission, make core−shell plasmonic nanohelices a powerful nanophotonic tool for, for example, (bio)sensing applications.

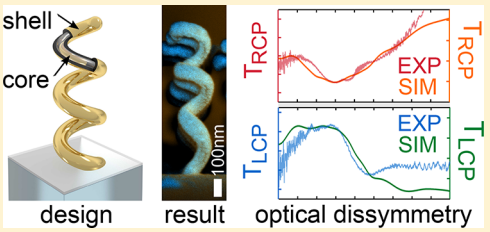

KEYWORDS: *chirality, nanohelices, plasmonics, core−shell, electron beam induced deposition*

Chiral photonic structures that control circular light fields, often on a chip, are becoming integral to quantum optical[1] and biosensing[2,3] technologies. Initially, chiral structures were microns in size and operated in the mid- or near-infrared.[4,5] Shrinking these to the nanoscale, for an optical response in the visible, proved challenging, but was ultimately possible when researchers turned to plasmonics.[6−16] In fact, nanoplasmonic structures are not only smaller, but they also enhance inherently weak chiral light−matter interactions and can even support superchiral light fields.[2,3,17]

One of the key aspects of nanoplasmonics is that, at the nanoscale, the optical properties of a structure can be controlled by geometry and not just its material properties. Indeed, chiral plasmonic nanostructures can be tuned by changing their size.[10,12,18−21] There are, however, few parameters that can be tuned on these structures, and changing even one can change the optical response in many different ways. Increasing the height can, for example, change both the center wavelength and amplitude of the optical response.[10] It is, therefore, difficult to tailor chiral plasmonic nanostructures to specific applications.

A transition from metallic to core−shell nanostructures would provide the requisite tunability while maintaining the plasmonic enhancement,[22−25] which is so crucial to applications. Yet, such a transition is far from trivial and, until now, nanostructures with both chiral cores and shells have not been successfully fabricated. Sensing this need, scientists have taken the first step, using a clever two-step evaporation process to create a chiral core−shell structure that consists of an achiral dielectric core surrounded by a partial metal shell.[26] It is only this shell that causes chirality of the entire structure, and hence, the tunability of this system is still relatively limited.

We report on the rapid and precise fabrication of plasmonic core−shell nanohelices, where both core and shell are chiral. Such helices, which are sketched in Figure 1a, are described by many geometric parameters that we can tune tune with nanometer accuracy. Here, we create arrays of thousands of core−shell nanohelices, and then use transmission measurements to demonstrate their asymmetrical response to visible light with different handedness. From these measurements we calculate a dissymmetry factor of 0.86, more than 2× larger

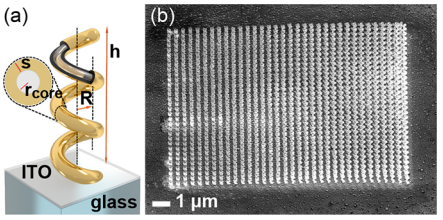

Figure 1. (a) Three-dimensional model of a core−shell nanohelix with the helix height h, major radius R, wire radius of the glass core r_{core}, and gold shell thickness s indicated. The helix stands on a glass substrate with a thin layer of ITO. (b) SEM of an array consisting of 1088 left-handed core−shell nanohelices spaced 400 nm apart. The array has dimensions 12.8 μm × 13.6 μm.

Received: May 17, 2017
Published: June 13, 2017

DOI: 10.1021/acsphotonics.7b00496
ACS Photonics 2017, 4, 1858−1863

than any reported to date. To demonstrate our control over the optical response of the nanohelices, we tune the amplitude of their resonance while holding its spectral position steady, in the visible, then use numerical simulations to discuss how the reverse situation may be achieved.

PLASMONIC NANOHELICES IN THE VISIBLE

We fabricate arrays of thousands of core−shell nanohelices, an example of which is displayed in Figure 1b. As the core of one nanohelix is fabricated in only 2.5 s, this 12.8 μm × 13.6 μm array of 1088 glass helices requires just 45 min. The shape of each helix (Figure 1a) is determined by its major radius R, core radius r_{core}, height h, the number of turns m, and the thickness of the gold shell s, and each of these parameters influences the optical response of the helix in a unique way.

The particular array shown in Figure 1b, which was designed to operate in the visible, is characterized by $m = 3$, $R = 80 \pm 15$ nm, $r_{core} = 25 \pm 10$ nm, $h = 655 \pm 110$ nm, and $s = 20 \pm 1$ nm. The spread in these parameters has been determined through multiple SEM measurements, and is indicative of how the helix shape varies across the whole array. It is only in the case of m, R, and s that these errors truly indicate the spread between nominally identical helices, as these parameters were held constant during fabrication. In contrast, h and r_{core} were systematically varied across the array (see SI, section 1) to subtly tune the optical response of the helices. In the case of h, the difference between nominally identical helices was only 40 nm, while a similar difference in r_{core} was below our measurement resolution.

We shine a focused (focus diameter 3 μm full-width at half-maximum, covering roughly 45 helices) circularly polarized, broadband light beam, which spans the visible and reaches into the near-infrared, through our nanohelix array. These transmission measurements, a typical example of which is shown in Figure 2a, show that there is a clear difference in which the nanohelices interact with left circular polarized (LCP, red curve) and right circular polarized (RCP, blue curve) light. Near 700 nm, in particular, our array of left-handed nanohelices transmits most of the incident LCP light, while blocking most incident RCP light. Since the transmission shown here, T_{exp}, is normalized to transmission through an adjacent region of flat gold film of thickness s, it can easily exceed unity, meaning that for certain wavelengths the array of nanohelices is more transparent to LCP light than is the planar film next to the array (see SI, section 2).

The asymmetry of the optical response of our nanohelix array to RCP and LCP beams is well reproduced by finite-difference time-domain (FDTD, see Method section) calculations, which we present in Figure 2b. Here, the calculated transmitted spectra T_{sim} through the helix array with $r_{core} = 15$ nm, $R = 80$ nm, $h = 600$ nm, and $s = 14$ nm, normalized to the incident illumination, can be seen to excellently reproduce the salient features of the experimental data (Figure 2a). Near 700 nm, for example, we again observe a dip in the transmission of RCP light and enhanced transmission of LCP light. As in the experimental data, we also observe a crossing of the two transmission spectra near 800 nm, after which more RCP light is transmitted.

To quantify the asymmetrical response of our nanohelix array to light with different handedness we calculate the differential transmission,

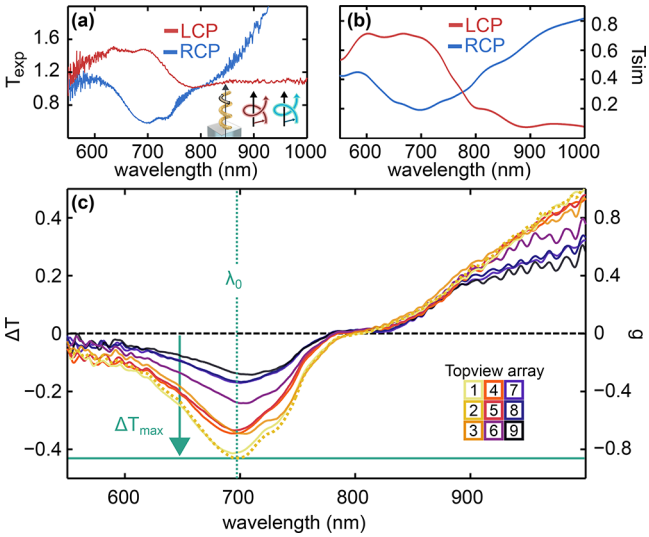

Figure 2. (a) Typical normalized transmission curve of right-handed circularly polarized light (RCP, blue) and left-handed circularly polarized light (LCP, red) through the nanohelices. In the inset, the polarization direction is indicated by the helical trace. (b) Results from FDTD simulation. (c) ΔT and g spectra determined for transmission measurements at nine different locations on the sample demonstrate the different response of the helices to RCP and LCP light. The dashed golden line corresponds to location 2 and is calculated with the data from graph (a).

$$\Delta T = \frac{T_{RCP} - T_{LCP}}{T_{RCP} + T_{LCP}} \quad (1)$$

presenting the results in Figure 2c. Here, the golden dashed curve represents ΔT for the data depicted in Figure 2a, which was measured at position 3 of the array (as shown in the inset). As expected, ΔT of this curve has a negative value below 800 nm, of which value peaks at $\Delta T_{max} = -0.43$ near 700 nm; at longer wavelengths, where $T_{RCP} > T_{LCP}$, the sign of ΔT flips, becoming positive. Transmission measurements at other positions of the helix array result in a smooth change of ΔT_{max} from this maximal value down to −0.14, while the central wavelength of the response, λ_0, remains virtually unaltered near 700 nm. As we discuss below, in the next section, this change in the optical response of the nanohelix array arises mainly from small changes to h and r_{core}, which we introduced during fabrication.

In Figure 2c we also show the dissymmetry factor (right axis), $g = 2\Delta T$ (ref 12), that, along with the ellipticity $\theta = \arctan[(\sqrt{T_{RCP}} - \sqrt{T_{LCP}})/(\sqrt{T_{RCP}} + \sqrt{T_{LCP}})]$ (ref 10), allow us to compare the performance of our core−shell nanohelices to previous chiral structures in the literature. For our glass-gold nanohelices, we find a maximum value of $|g| = 0.86$ (and a corresponding $\theta = 13°$) at λ_0. It is not surprising that this value is many orders of magnitude larger than that of chiral molecules, where $|g|$ ranges from 10^{-7} to 10^{-5} (ref 27). It is, however, very promising that our measured $|g|$ is more than two times larger than previously measured dissymmetry factors of plasmonic nanostructures.[10,12] Moreover, without further optimization, our calculations (Figure 2b) demonstrate that $|g| = 1.1$ (and $|\theta| > 15°$) are possible with our geometry (see SI, section 5).

DOI: 10.1021/acsphotonics.7b00496
ACS Photonics 2017, 4, 1858−1863

FABRICATION OF 3D NANOSCOPIC AND CHIRAL CORE–SHELL STRUCTURES

A two-step process allows us to fabricate core–shell nanohelices consisting of a chiral core and a uniform shell in a fast, accurate and reproducible manner. We first use electron beam induced deposition (EBID) to fabricate the glass core and subsequently sputter coat the gold shell.[28] EBID can be used to fabricate complex three-dimensional nanostructures with high resolution at precisely defined locations.[28−34] In our case, EBID confers nanometer control over the core radius, major radius and height of the helices. Sputter coating then creates a conformal metal shell on the core. Both EBID and sputter coating techniques are known to work with a wide variety of materials. While EBID is less common, it has been used for over 50 years and it just requires addition of a commercially available GIS to a standard scanning electron microscope.[31] Nowadays, EBID is used to fabricate complex three-dimensional nanostructures.[35]

Electron beam induced deposition is based on a reaction between a precursor gas and an electron beam near a substrate that causes the precursor gas molecules to locally dissociate into a nonvolatile deposit and a volatile side product. This process is schematically depicted in Figure 3a. The structure is, in effect, created only in the presence of the electron beam, whose dimensions and position can be controlled with nanometer precision. Scanning this beam can then create complex three-dimensional geometries. For example, holding the beam in one position deposits a vertical rod, while tracing m circles leads to deposition of a helix with m turns. In our work, the electron beam comes from a FEI Helios Nanolab 600 SEM, and a combination of tetraethoxysilane (TEOS) precursor gas with water vapor results in SiO_x deposits,[31,33] a silica-like oxide we hereafter refer to as glass.

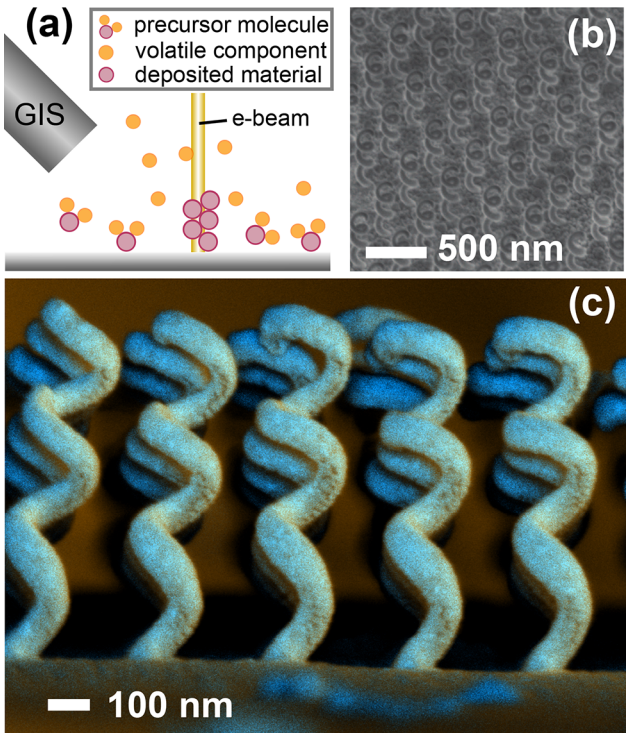

Figure 3. (a) Schematic representation of electron beam induced deposition (EBID) that is used to fabricate the glass helix. Where the e-beam of a SEM hits the substrate, glass is deposited due to the presence of the precursor gas TEOS provided by a gas injection system (GIS). Volatile components are removed from the vacuum chamber of the SEM (b) Nanoscale glass helices fabricated with EBID. (c) Core–shell (glass-gold) nanohelices after sputter coating. The overlay of images from two different detectors provides compositional information: blue represents gold and black represents glass.

The shape and size of the glass helices depends on a delicate interplay between several parameters including the electron beam energy, electron beam current, dwell time, step size and location with respect to the gas injection system (GIS) that provides the precursor.[12,31,33,36] Of these, the nanohelix geometry is particularly sensitive to the dwell time and step size of the electron beam, and its distance from the GIS. The first, the dwell time, is the time that the electron beam resides at one position and increasing this parameter increases the amount of deposited material. The second, the step size, is the distance between two successive points where the e-beam is placed and it must be precisely set for helices to form. Setting a too small, or too large, value for the step size results in either pillars or planar circles, respectively (see SI, section 3). Lastly, the distance from the GIS determines the amount of precursor available, and hence the amount of material that will be deposited.[37] In this work, we hold the step size and dwell time constant (see SI, section 1 and Figure S1) while slowly varying the distance to the GIS, allowing us to subtly tune h and r_{core} of successive helices, creating arrays with position-dependent optical responses. In practice, one could also hold all parameters constant to produce arrays of identical helices for targeted applications.

The SEM image in Figure 3b shows glass helices, fabricated with an electron beam energy of 1 keV, an electron beam current of 21 pA, a dwell time of 14 ms, a step size of 5 nm and a chamber pressure of 1.4×10^{-5} mbar. Under these conditions, the growth of a single glass nanohelix takes approximately 2.5 s, meaning that the fabrication of the array of 1088 nanohelices shown in Figure 3b, which covers an area of ~175 μm^2, takes roughly 45 min. This duration is comparable to that required to fabricate a similar array of pure metal nanohelices by glancing angle deposition, where all nanohelices are grown simultaneously.[10,20,38] However, by using EBID we could, in principle, choose the size parameters of every single helix in the array at no additional time cost.

We then conformally coat the nanohelix cores with a gold shell via sputter coating.[28] The false color image in Figure 3c reveals the resulting gold coverage. Here, the gold is shown in blue and the glass core in black. We observe that the gold coverage of the bottom of the helices is less homogeneous than on the top, perhaps explaining some of the differences in the details between the optical measurements and the numerical simulations (of the idealized helices) presented in Figure 2.

There are several advantages to the sputter deposition of gold, in comparison with EBID of gold nanostructures. First, by sputter coating we can control s much more finely than with EBID. Second, and perhaps more importantly, currently available Au-precursors only allow for the deposition of heavily contaminated gold (atomic fraction of Au up to only 60% have been reported), which degrades the optical properties of the nanostructures.[39−44] In contrast, the gold target used for sputter coating is up to 99.99% pure and, hence, so is the golden shell of our nanohelices

DOI: 10.1021/acsphotonics.7b00496
ACS Photonics 2017, 4, 1858−1863

TUNABILITY OF CORE−SHELL NANOHELICES

To better understand the dependence of the optical response of the nanohelix array on its geometric parameters, we use FDTD simulations to calculate ΔT for different helix shapes. In each of our simulations we calculate successive ΔT spectra while sweeping one of the geometric parameters from a fixed set of parameters, which we refer to as the baseline, of m = 3, r_{core} = 15 nm, R = 80 nm, h = 600 nm, and s = 14 nm and assuming that our helices are ideal (e.g., with a homogeneous gold shell). We begin by gradually changing r_{core} and h in our simulations to reflect our experimental sample geometry (see first section), showing the resultant ΔT spectra in Figure 4a,b. Recall that the

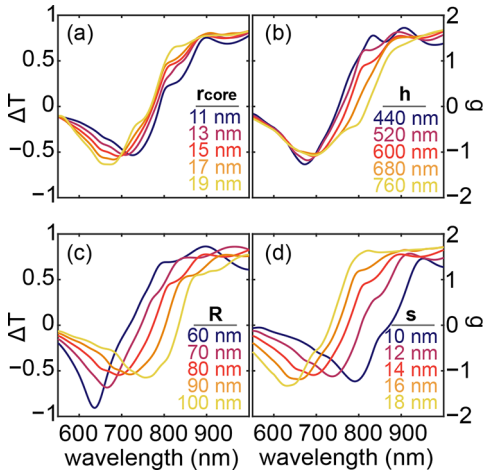

Figure 4. Simulation results of ΔT versus wavelength for four geometrical parameter sweeps: radius of the core, r_{core}, major radius R, height h, and gold shell thickness s. (a) Results for variation of the radius of the core, r_{core}. Five different radii were simulated, represented by different colors, while keeping other three geometrical parameters constant. (b) Variation of major radius R. (c) Variation of height h. (d) Variation of gold shell thickness s.

baseline spectra in these images (red curve) is identical to that presented in Figure 2b. Interestingly, these simulations reveal that both the amplitude and λ_0 of the optical response of the nanohelices depend weakly on r_{core} and h. A closer inspection, however, reveals that small variations in h can result in a change of ΔT_{max} for a roughly constant λ_0 and that the shift introduced by larger height changes may still be counteracted by simultaneous changes to r_{core}; that is, lengthening the helices leads to a red shift of the ΔT spectrum, while thickening the helices results in a blue shift.

The major radius and shell thickness of the core−shell nanohelices provide additional degrees of freedom that may be exploited to control the optical response of these nanostructures. Indeed, changing R and s can produce a much more dramatic effect on ΔT than does changing r_{core} or h, as we observe in Figure 4c,d. In particular, we note that changing either R or s can result in shifts of λ_0 of more than 100 nm, even when the R changes by as little as 40 nm and s by 8 nm. Note that the spectral shift in ΔT due to change of s is in the same direction as the resonance shift for a straight core−shell nanowire, but much larger (see SI, section 4). This suggests that using such core−shell nanohelices it becomes possible to shift the ΔT spectrum while keeping its amplitude constant, for example, by primarily changing s and then using fine adjustments to the remaining three parameters to counteract any amplitude variations. By carefully designing these nanohelices, one can in principle target any wavelength within 100s of nanometers, both in the visible and near infrared.

CONCLUSIONS

To conclude, we show how large arrays of thousands of plasmonic core−shell nanohelices can be rapidly and precisely fabricated. Transmission measurements show that the asymmetry in the response of the helices to light of different circular polarization peaks at the edge of the visible spectrum, near 700 nm, where we measure $|g|$ = 0.86. The measured dissymmetry factor is already more than twice the magnitude previously reported in literature, and FDTD simulations reveal that $|g| \approx 2$ is possible with our geometry. Therefore, as these nanohelices have a strong far-field chiral optical response, they are predicted to have an enhanced local (near-field) optical chirality,[45] directly resulting in an enhanced interaction with chiral molecules, beneficial to a (bio)sensing application.[17] Due to the complexity of the chiral response and the nontrivial effect of every single geometrical parameter, we suggest that optimization for a certain response will require state-of-the-art algorithms, like genetic algorithms.[46] Our measurements show that it is possible to change $|g|$ by subtly tuning the helix geometry, while keeping the spectral position of the optical response constant. Likewise, numerical simulations suggest that it is also possible to hold $|g|$ constant while shifting the center of the optical response by over 100 nm, making these plasmonic core−shell nanohelices promising candidates for future biosensing applications.[2,3]

METHOD

Transmission Measurements. A continuum white light laser (source) provides broad range of wavelengths (λ = 550−1000 nm) for the transmission measurements. The light is circularly polarized using a linear polarizer (LP) and a quarter wave plate (QW), then focused onto the sample with a 40× objective to a spot with full width half-maximum of 3 μm. The sample is illuminated from below, such that the light first travels through the substrate and then through the array of nanohelices. The transmission is collected with a second (collection) 40× objective then sent to grating spectrometer. A pellicle beam splitter (PB) and flip mirror (FM) are used for navigation over the sample (Figure 5).

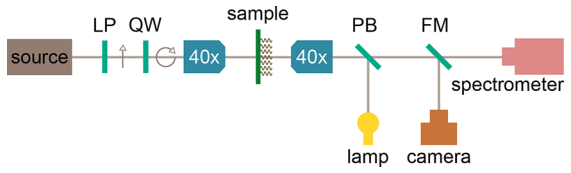

Figure 5. Setup of the transmission measurements (see text).

FDTD Simulations. The FDTD model is created using Lumerical Computational Solutions (Figure 6). A core−shell nanohelix is modeled using a stack of cylinders. For one pitch of 200 nm height, 250 cylinders are used. The end facet of the helix is rounded by adding a glass and gold sphere. Data from Johnson and Christy[47] is used for the dielectric constant of gold. Glass is modeled with a refractive index of 1.5. Periodic boundary conditions (PBC) in x- and y-directions at 400 nm distance create the square lattice. In the z-direction, the boundary is a perfectly matched layer (PML). Several mesh

DOI: 10.1021/acsphotonics.7b00496
ACS Photonics 2017, 4, 1858−1863

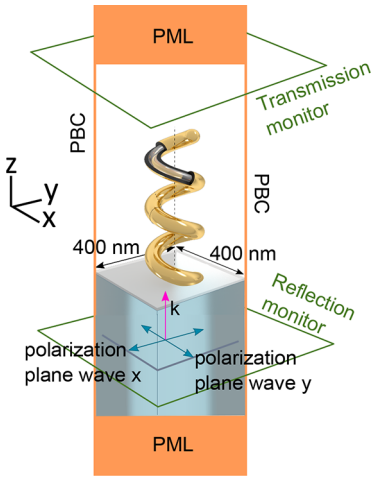

Figure 6. Setup of the FDTD model (see text).

checks are performed and conformal variant 2 is used as mesh refinement combined with a mesh size of $1 \times 1 \times 1$ nm^3 in the area surrounding the helix and a mesh size of $2 \times 2 \times 1$ nm^3 surrounding the interface between the substrate and air. Two plane-wave sources with a phase difference of $\pi/2$ and polarized at an angle of 90° are used to create circularly polarized light traveling in the z-direction (k). Two frequency domain power monitors are used to determine reflection and transmission coefficients in the far-field. As the incident plane wave has amplitude 1, the transmission, reflection, and absorption are normalized by 1.

■ ASSOCIATED CONTENT

Supporting Information

The Supporting Information is available free of charge on the ACS Publications website at DOI: 10.1021/acsphotonics.7b00496.

Detailed SEM images of helices with varying height and core radius, additional information from reference transmission measurements, details on the parameters explored for successful electron beam induced deposition of nanohelices, results from a reference 2D simulation of a straight core−shell nanowire of equal dimensions, and calculations of dissymmetry factor g and ellipticity θ (PDF).

■ AUTHOR INFORMATION

Corresponding Author

*E-mail: l.kuipers@tudelft.nl.

ORCID

Dolfine Kosters: 0000-0001-5465-6222

L. Kuipers: 0000-0003-0556-8167

Notes

The authors declare no competing financial interest.

■ ACKNOWLEDGMENTS

The authors thank D. Norris and H. Giessen for valuable discussions and S. Mann for help with the simulations. This work is part of the research programme of The Netherlands Organisation for Scientific Research (NWO). This work was funded by ERC Advanced Investigator Grant (No. 340438-CONSTANS).

■ REFERENCES

(1) Söllner, I.; Mahmoodian, S.; Hansen, S. L.; Midolo, L.; Javadi, A.; Kiršanskė, G.; Pregnolato, T.; El-Ella, H.; Lee, E. H.; Song, J. D.; Stobbe, S.; Lodahl, P. Deterministic photon-emitter coupling in chiral photonic circuits. *Nat. Nanotechnol.* **2015**, *10*, 775−778.

(2) Tang, Y.; Cohen, A. E. Enhanced enantioselectivity in excitation of chiral molecules by superchiral light. *Science* **2011**, *332*, 333−6.

(3) Hendry, E.; Carpy, T.; Johnston, J.; Popland, M.; Mikhaylovskiy, R. V.; Lapthorn, A. J.; Kelly, S. M.; Barron, L. D.; Gadegaard, N.; Kadodwala, M. Ultrasensitive detection and characterization of biomolecules using superchiral fields. *Nat. Nanotechnol.* **2010**, *5*, 783−7.

(4) Gansel, J. K.; Thiel, M.; Rill, M. S.; Decker, M.; Bade, K.; Saile, V.; von Freymann, G.; Linden, S.; Wegener, M. Gold helix photonic metamaterial as broadband circular polarizer. *Science* **2009**, *325*, 1513−1515.

(5) Hentschel, M.; Schäferling, M.; Weiss, T.; Liu, N.; Giessen, H. Three-dimensional chiral plasmonic oligomers. *Nano Lett.* **2012**, *12*, 2542−7.

(6) Fan, Z.; Govorov, A. O. Plasmonic circular dichroism of chiral metal nanoparticle assemblies. *Nano Lett.* **2010**, *10*, 2580−2587.

(7) Fan, Z.; Govorov, A. O. Helical Metal Nanoparticle Assemblies with Defects: Plasmonic Chirality and Circular Dichroism Helical Metal Nanoparticle Assemblies with Defects: Plasmonic Chirality and Circular Dichroism. *J. Phys. Chem. C* **2011**, *115*, 13254−13261.

(8) Ma, W.; Kuang, H.; Xu, L.; Ding, L.; Xu, C.; Wang, L.; Kotov, N. A. Attomolar DNA detection with chiral nanorod assemblies. *Nat. Commun.* **2013**, *4*, 2689.

(9) Frank, B.; Yin, X.; Scha, M.; Zhao, J.; Hein, S. M.; Braun, P. V.; Giessen, H. Large-Area 3D Chiral Plasmonic Structures. *ACS Nano* **2013**, *7*, 6321−6329.

(10) Gibbs, J. G.; Mark, A. G.; Eslami, S.; Fischer, P. Plasmonic nanohelix metamaterials with tailorable giant circular dichroism. *Appl. Phys. Lett.* **2013**, *103*, 213101.

(11) Song, C.; Blaber, M. G.; Zhao, G.; Zhang, P.; Fry, H. C.; Schatz, G. C.; Rosi, N. L. Tailorable Plasmonic Circular Dichroism Properties of Helical Nanoparticle Superstructures. *Nano Lett.* **2013**, *13*, 3256−3261.

(12) Esposito, M.; Tasco, V.; Cuscunà, M.; Todisco, F.; Benedetti, A.; Tarantini, I.; Giorgi, M. D.; Sanvitto, D.; Passaseo, A. Nanoscale 3D Chiral Plasmonic Helices with Circular Dichroism at Visible Frequencies. *ACS Photonics* **2015**, *2*, 105−114.

(13) Eslami, S.; Gibbs, J. G.; Rechkemmer, Y.; van Slageren, J.; Alarcón-Correa, M.; Lee, T.-C.; Mark, A. G.; Rikken, G. L. J. A.; Fischer, P. Chiral Nanomagnets. *ACS Photonics* **2014**, *1*, 1231−1236.

(14) Caridad, J. M.; McCloskey, D.; Rossella, F.; Bellani, V.; Donegan, J. F.; Krstić, V. Effective Wavelength Scaling of and Damping in Plasmonic Helical Antennae. *ACS Photonics* **2015**, *2*, 675−679.

(15) Kolkowski, R.; Petti, L.; Rippa, M.; Lafargue, C.; Zyss, J. Octupolar plasmonic meta-molecules for nonlinear chiral water-marking at subwavelength scale. *ACS Photonics* **2015**, *2*, 899−906.

(16) Wang, L.-Y.; Smith, K. W.; Dominguez-Medina, S.; Moody, N.; Olson, J. M.; Zhang, H.; Chang, W.-S.; Kotov, N.; Link, S. Circular Differential Scattering of Single Chiral Self-Assembled Gold Nanorod Dimers. *ACS Photonics* **2015**, *2*, 1602−1610.

(17) Tang, Y.; Cohen, A. E. Optical chirality and its interaction with matter. *Phys. Rev. Lett.* **2010**, *104*, 163901.

(18) Gansel, J. K.; Wegener, M.; Burger, S.; Linden, S. Gold helix photonic metamaterials: a numerical parameter study. *Opt. Express* **2010**, *18*, 1059−69.

(19) Kuzyk, A.; Schreiber, R.; Fan, Z.; Pardatscher, G.; Roller, E.-M.; Högele, A.; Simmel, F. C.; Govorov, A. O.; Liedl, T. DNA-based self-assembly of chiral plasmonic nanostructures with tailored optical response. *Nature* **2012**, *483*, 311−4.

(20) Mark, A. G.; Gibbs, J. G.; Lee, T.-C.; Fischer, P. Hybrid nanocolloids with programmed three-dimensional shape and material composition. *Nat. Mater.* **2013**, *12*, 802−7.

DOI: 10.1021/acsphotonics.7b00496
ACS Photonics 2017, 4, 1858−1863

(21) Schäferling, M.; Dregely, D.; Hentschel, M.; Giessen, H. Tailoring Enhanced Optical Chirality: Design Principles for Chiral Plasmonic Nanostructures. *Phys. Rev. X* **2012**, *2*, 031010.
(22) Prodan, E.; Radloff, C.; Halas, N. J.; Nordlander, P. A Hybridization Model for the Plasmon Response of Complex Nanostructures. *Science* **2003**, *302*, 419−423.
(23) Prodan, E.; Nordlander, P.; Halas, N. J. Electronic Structure and Optical Properties of Gold Nanoshells. *Nano Lett.* **2003**, *3*, 1411−1415.
(24) Wang, H.; Brandl, D. W.; Le, F.; Nordlander, P.; Halas, N. J. Nanorice: A Hybrid Plasmonic Nanostructure. *Nano Lett.* **2006**, *6*, 827−832.
(25) Lal, S.; Link, S.; Halas, N. J. Nano-optics from sensing to waveguiding. *Nat. Photonics* **2007**, *1*, 641−648.
(26) Yeom, B.; Zhang, H.; Zhang, H.; Park, J. I.; Kim, K.; Govorov, A. O.; Kotov, N. A. Chiral plasmonic nanostructures on achiral nanopillars. *Nano Lett.* **2013**, *13*, 5277−83.
(27) Barron, L. D. *Molecular Light Scattering and Optical Activity*; Cambridge University Press: New York, NY, 1982.
(28) Acar, H.; Coenen, T.; Polman, A.; Kuipers, L. Dispersive ground plane core-shell type optical monopole antennas fabricated with electron beam induced deposition. *ACS Nano* **2012**, *6*, 8226−32.
(29) Silvis-Cividjian, N. Electron Beam Induced Nanometer Scale Deposition. *Ph.D. thesis*, TU Delft, 2002.
(30) van Dorp, W. F.; van Someren, B.; Hagen, C. W.; Kruit, P.; Crozier, P. Approaching the resolution limit of nanometer-scale electron beam-induced deposition. *Nano Lett.* **2005**, *5*, 1303−7.
(31) Randolph, S. J.; Fowlkes, J. D.; Rack, P. D. Focused, Nanoscale Electron-Beam-Induced Deposition and Etching. *Crit. Rev. Solid State Mater. Sci.* **2006**, *31*, 55−89.
(32) Danelon, C.; Santschi, C.; Brugger, J.; Vogel, H. Fabrication and functionalization of nanochannels by electron-beam-induced silicon oxide deposition. *Langmuir* **2006**, *22*, 10711−10715.
(33) van Dorp, W. F.; Hagen, C. W.; Crozier, P. A.; Kruit, P. Growth behavior near the ultimate resolution of nanometer-scale focused electron beam-induced deposition. *Nanotechnology* **2008**, *19*, 225305.
(34) van Kouwen, L.; Botman, A.; Hagen, C. W. Focused electron-beam-induced deposition of 3 nm dots in a scanning electron microscope. *Nano Lett.* **2009**, *9*, 2149−52.
(35) Fowlkes, J. D.; Winkler, R.; Lewis, B. B.; Stanford, M. G.; Plank, H.; Rack, P. D. Simulation-Guided 3D Nanomanufacturing via Focused Electron Beam Induced Deposition. *ACS Nano* **2016**, *10*, 6163−6172.
(36) Reimer, L. *Scanning Electron Microscopy*; Springer-Verlag: Berlin, 1998.
(37) Winkler, R.; Fowlkes, J.; Szkudlarek, A.; Utke, I.; Rack, P. D.; Plank, H. The Nanoscale Implications of a Molecular Gas Beam during Electron Beam Induced Deposition. *ACS Appl. Mater. Interfaces* **2014**, *6*, 2987−2995.
(38) Caridad, J. M.; McCloskey, D.; Donegan, J. F.; Krstić, V. Controllable growth of metallic nano-helices at room temperature conditions. *Appl. Phys. Lett.* **2014**, *105*, 233114.
(39) Utke, I.; Hoffmann, P.; Dwir, B.; Leifer, K.; Kapon, E.; Doppelt, P. Focused electron beam induced deposition of gold. *J. Vac. Sci. Technol., B: Microelectron. Process. Phenom.* **2000**, *18*, 3168.
(40) Mølhave, K.; Madsen, D. N.; Rasmussen, A. M.; Carlsson, A.; Appel, C. C.; Brorson, M.; Jacobsen, C. J. H.; Bøggild, P. Solid Gold Nanostructures Fabricated by Electron Beam Deposition. *Nano Lett.* **2003**, *3*, 1499−1503.
(41) Botman, A.; Mulders, J.; Weemaes, R.; Mentink, S. Purification of platinum and gold structures after electron-beam-induced. *Nanotechnology* **2006**, *17*, 3779−3785.
(42) Höflich, K.; Yang, R. B.; Berger, A.; Leuchs, G.; Christiansen, S. The Direct Writing of Plasmonic Gold Nanostructures by Electron-Beam-Induced Deposition. *Adv. Mater.* **2011**, *23*, 2657−2661.
(43) van Dorp, W. F.; Wu, X.; Mulders, J. J. L.; Harder, S.; Rudolf, P.; Hosson, J. T. M. D. Gold Complexes for Focused-Electron-Beam-Induced Deposition. *Langmuir* **2014**, *30*, 12097−12105.
(44) Belić, D.; Shawrav, M. M.; Gavagnin, M.; Stöger-Pollach, M.; Wanzenboeck, H. D.; Bertagnolli, E. Direct-Write Deposition and Focused-Electron-Beam-Induced Purification of Gold Nanostructures. *ACS Appl. Mater. Interfaces* **2015**, *7*, 2467−2479.
(45) Poulikakos, L. V.; Gutsche, P.; McPeak, K. M.; Burger, S.; Niegemann, J.; Hafner, C.; Norris, D. J. Optical Chirality Flux as a Useful Far-Field Probe of Chiral Near Fields. *ACS Photonics* **2016**, *3*, 1619−1625.
(46) Wiecha, P. R.; Arbouet, A.; Girard, C.; Lecestre, A.; Larrieu, G.; Paillard, V. Evolutionary multi-objective optimization of colour pixels based on dielectric nanoantennas. *Nat. Nanotechnol.* **2016**, 1−10.
(47) Johnson, P. B.; Christy, R. W. Optical Constants of the Noble Metals. *Phys. Rev. B* **1972**, *6*, 4370−4379.

DOI: 10.1021/acsphotonics.7b00496
ACS Photonics 2017, 4, 1858−1863